International Journal of Applied Mechanics
Vol. 2, No. 2 (2010) 1–15
© Imperial College Press
DOI: 10.1142/S1758825110000603

LES AND 'IN-VITRO' EXPERIMENTAL VALIDATION OF FLOW AROUND A TEETH-SHAPED OBSTACLE

ANNEMIE VAN HIRTUM*, XAVIER GRANDCHAMP
and XAVIER PELORSON

Gipsa-lab, UMR 5216 CNRS
Grenoble Universities
961 rue de la Houille Blanche
BP 46, France

KAZUNORI NOZAKI† and SHINJI SHIMOJO

Cybermedia Center
Osaka University
Japan

Received
Accepted

The current paper aims to provide numerical and experimental flow data relevant for physical modelling of human fricative sound production due to the interaction of airflow with the teeth. A simplified upper incisor-palate geometry is derived from typical morphological features. The geometry is inserted in a rectangular channel for which the width-to-height ratio yields 4. The obstruction degree due to the presence of the simplified upper incisor yields 70%. Numerical flow data are obtained from large eddy simulations. Experimental flow data are gathered from single-sensor anemometry on a rigid plaster print of the computational grid. Transverse velocity profiles are obtained downstream the constricted area, i.e. from $x = 0$ up to $x/h = 1.5$ with h denoting the aperture height. The Reynolds number is set to 4000. The mean velocity profiles derived on simulated and measured data exhibit a strong asymmetry due to the presence of the obstruction. Nevertheless, significant differences appear with respect to the jet development, as e.g., quantified by the downstream evolution of the jet width or the appearance of significant turbulence intensities (>10%) at the teeth edge in the measured data whereas the simulated flow remains laminar.

Keywords: Anemometry; LES; teeth-shaped obstacle; two-dimensional jet.

1. Introduction

Morphological teeth features, such as their exact position, orientation and shape, influence human fricative sound production [Runte *et al.*, 2001]. As a consequence, morphological features are of particular interest for dental prosthesis design and

*Cybermedia Center, Osaka University, Japan.
†The Center for Advanced Medical Engineering and Informatics, Osaka University, Japan.

well documented in literature [Pound, 2001; Schierano *et al.*, 2001; McIntyre and Millett, 2003, 2006; Rudolph *et al.*, 1998; Heydecke *et al.*, 2004].

In addition to available morphological characteristics, technologies such as Cone Beam CT scans, e.g., used for clinical diagnoses in dental practise, are assessed to obtain three-dimensional patient-specific reconstructions of oral cavity portions. Such reconstructions are in particular useful for personalised grid reconstruction aiming personalised computational aero-acoustic studies [Nozaki *et al.*, 2005]. Nevertheless, resulting flow and acoustic data need to be validated before applying such computational results for medical purposes such as dental practice.

In sharp contrast to morphological data, flow data issuing from configurations relevant to human fricative production, i.e. moderate Reynolds Re and low Mach Ma number, are few. Obviously, model validation would benefit from additional flow data providing quantitative information on the mean and turbulent part of the spatial velocity distribution as pointed out a.o. by Howe and McGowan [2005]. Recently, single sensor anemometry was applied to characterise the spatial velocity distribution of moderate Re and low Ma flow issuing from an extended conical diffuser [Van Hirtum *et al.*, 2009]. The data allowed to validate self-similar flow models, which are suitable to be applied to model the airflow issuing from a constriction between the tongue and the palatal plane. Although, no obstacle was considered and no computational results were provided.

'In-vitro' mechanical models of simplified geometries suitable to study fricative sound production are few. A rectangular obstacle downstream an obstruction was considered by Shadle [1985] in order to study the influence on the sound produced, so no detailed velocity flow data were gathered.

The present research aims to provide velocity data downstream an incisor-shaped obstacle in a rectangular uniform vocal tract for an airflow with moderate Re-number set to $Re = 4000$. The chosen Reynolds number is well within the range typical for fricative sound production $2000 < Re < 10^4$ [Stevens, 1998; Howe and McGowan, 2005]. The obstruction degree yields 70% and the width-to-height ratio is set to 4 to ensure two-dimensional flow. A comparison of experimental and numerical mean and turbulent velocity data is provided in the near flow field downstream the obstacle from $x = 0$ up to $x/h = 1.5$ where h denotes the aperture. Both the inner and outer layers of the jet issuing from the aperture are sought. The characterisation is inspired on features commonly observed for plane wall jets since a two-layer shear flow can be expected [Launder and Rodi, 1983; Eriksson *et al.*, 1998; Townsend, 1999].

2. Geometry of Interest: Palate-Teeth Shaped Obstacle and Nozzle

Dental dimensions and measures are reported in literature with increasing precision. High precision is required for sophisticated dental surgical techniques and the development of personalized denture services such as dental prosthesis. In this section, a simplified two-dimensional teeth-shaped obstacle geometry is derived from reported

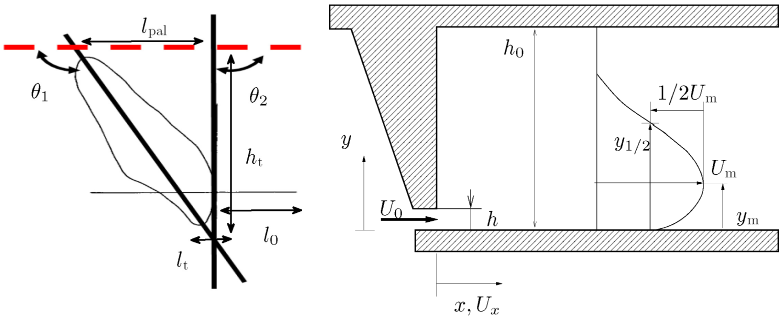

(a) Obstacle (b) Nozzle

Fig. 1. Schematic illustration of (a) two-dimensional teeth-shaped obstacle (bold lines) in relation to upper incisor morphological data [Fredericks, 1974; Ellis and McNamara, 1986]: the palatal plane is indicated as a dashed line and (b) resulting teeth-shaped nozzle and some major geometrical and flow parameters derived from plane wall jet nomenclature [Eriksson *et al.*, 1998]: transverse flow direction y, longitudinal flow component $U_x(x)$ in the main flow direction x indicated by a bold arrow, characteristic velocity at the constriction outlet U_0 at $x \approx 0$, aperture height h , channel height h_0, $y_{\rm m}(x)$ distance from the wall up to the position of maximum flow velocity $U_{\rm m}(x)$ in the transversal velocity profile, $y_{1/2}(x)$ distance from the wall up to the outer position where the velocity corresponds to $U_{\rm m}/2(x)$.

upper teeth incisor measures. In the simplified geometry, schematically illustrated in Fig. 1, the palatal plane is represented by a flat plane and the upper teeth geometry is represented as a trapezoid connected to the palatal plane, i.e. the upper teeth consists of four straight plates. This way, in particular two morphological features are accounted for in the current upper teeth-shaped obstacle:

(1) upper incisor dimensions in the flow direction,
(2) upper teeth position with respect to the palatal plane.

Based on the incisor inclinations reported in Fredericks [1974] and Ellis and McNamara [1986] the angles of the trapezoid with respect to the palatal plane denoted θ_1 and θ_2 are set as: $\theta_1 = 107°$ and $\theta_2 = 90°$. The upper parallel side or the base of the trapezoid coincides with the palatal plane $l_{\rm pal}$ and the lower parallel side represents the teeth tip $l_{\rm t}$. The tip length in the main flow direction [Rudolph *et al.*, 1998] is set to $l_{\rm t} = 1.25$ mm and the height h_t [Magne *et al.*, 2003] is set to 17.5 mm which is within the range observed on 'in-vivo' data [Rudolph *et al.*, 1998; Magne *et al.*, 2003]. Consequently, the base of the trapezoid yields $l_{\rm pal} = 6.6$ mm. The distance indicated as l_0 in Fig. 1(a) corresponds morphologically to the distance between the trailing teeth edge and the trailing edge of the lips and is set to $l_0 \approx 1.7 \times l_{\rm pal} = 11$ mm based on the ratios between teeth width and trailing lip position reported by McIntyre and Millett [2003]. The mentioned upper-teeth dimensions provide a two-dimensional palate-teeth shaped obstacle.

Next, a three-dimensional teeth-shaped nozzle is obtained by inserting the two-dimensional palate-teeth shaped obstacle in a rectangular channel representing a portion of the vocal tract, for which the upper wall represents the hard palate, resulting in a teeth-shaped nozzle. A longitudinal view of the resulting nozzle is schematically illustrated in Fig. 1(b). The width w of the channel is fixed to $w = 105\,\text{mm}$ and the inlet height of the channel is set to $h_0 = 25\,\text{mm}$, so that the aspect ratios, both in the unconstricted and constricted region, are superior to 1, $w/h_0 \approx 4$ and $w/h \approx 14$ with $h = h_0 - h_t$ the aperture height. Consequently, the flow is expected to be two-dimensional. The contraction ratio h_0/h yields ≈ 3.3 resulting in a $\pm 70\%$ obstruction degree. The length of the channel downstream the constriction ranges from $x = 0$ up to $x/h = 1.5$.

3. Numerical Simulation of the Airflow Through the Nozzle

The airflow is simulated with Large Eddy Simulation (LES) for incompressible unsteady flows. The dynamic Smagorinsky model [Germano *et al.*, 1991] with modification due to Lilly [1992] is used so that the Smagorinsky coefficient C_s is determined locally in space and time. Simulations are obtained with a general-purpose finite element code *Front Flow Blue/FFB 5* on a supercomputer (SX8 NEC Inc.) [Kato and Ikegawa, 1991; Guo *et al.*, 2006].

The downstream section of the computational domain matches the teeth-shaped nozzle defined in Sec. 2. The simulation geometry upstream the teeth-shaped obstacle consists in a uniform rectangular section matching the channel height h_0 and width w of the teeth-shaped obstacle nozzle illustrated in Fig. 1(b). The total length upstream the teeth-shaped obstacle yields $3.2h_0$. Structured meshes are used to generate the computational grid of 18,82,200 elements (Gridgen v1.5, Pointwise Inc.). The grid meshes are refined close to and downstream the obstacle in order to resolve the boundary layer. The quality of the mesh was extensively verified as well as the Courant–Friedrichs–Lewy number during simulation. A uniform velocity profile is imposed at the inlet of the computational domain. No-slip boundary conditions are used at the wall whereas non-reflective conditions are imposed at the outlet. The averaged grid accuracy at and downstream of the constriction yields 0.13 mm and increases to 0.05 mm along the boundaries.

The non-dimensional time increment Δt is set so that $10^{-3} = \Delta t \cdot U_b/h_0$ with U_b the bulk velocity at the inlet and h_0 the unconstricted nozzle height. The Reynolds number is set to $Re = 4000$ so that the bulk velocity yields $U_b = 2.5\,\text{m/s}$. An overview of imposed geometrical and flow parameters is given in Table 1. Mean and fluctuating characteristics of the velocity field are quantified on 5000 instantaneous flow fields obtained from time step 5000 up to 10,000.

4. In-Vitro Experimental Setup and Nozzle

4.1. *'In-vitro' experimental conditions and nozzle*

Airflow is generated in a flow facility consisting of an air compressor (Atlas Copco GA7) followed by a manual valve and pressure regulator (Norgren type 11-818-987) enabling one to provide constant air pressure. A uniform duct of diameter

Table 1. Overview of flow conditions and nozzle characteristics for LES simulations and 'in-vitro' experiments.

	LES	'in-vitro'
Nozzle width, w	105 mm	
Nozzle length, l	97 mm	59.5 mm
Nozzle height, h_0	25.0 mm	
Nozzle wall thickness, th	0 mm	6 mm
Trailing obstacle edge from outlet, l_0	11.0 mm	
Tip length of the obstacle, l_t	1.25 mm	
Leading obstacle angle, θ_1	107°	
Trailing obstacle angle, θ_2	90°	
Minimum aperture, h	7.5 mm	
Inlet Reynolds number, Re	4000	
Inlet bulk velocity, U_b	2.5 m/s	
Volume airflow rate, ϕ	363 l/min	

1cm connects the pressure regulator to a short convergent-divergent diffuser with total length 7 cm and outlet diameter 25 mm. The diffuser is attached to a settling chamber of volume 0.12 m^3 with dimensions $600 \times 510 \times 415$ mm (length $\times$ width $\times$ height). Grids are used in the settling chamber to reduce turbulence intensity so that the streamwise turbulence intensity at the nozzle inlet is below 1%.

The rectangular rigid nozzle, described in Sec. 2, was mounted at the exit of the settling chamber. The constriction geometry is shaped in accordance with Sec. 2, so that the nozzle represents a simplified 'in-vitro' replica of a teeth-shaped obstacle in the upper airways. The resulting nozzle geometry and setup are schematically illustrated in Fig. 2. The main 'in-vitro' nozzle characteristics are summarised in Table 1. The nozzle geometry was obtained as a three-dimensional plaster print from the numerical grid (3D Digital Service OURA Inc.). Consequently, the 'in-vitro'

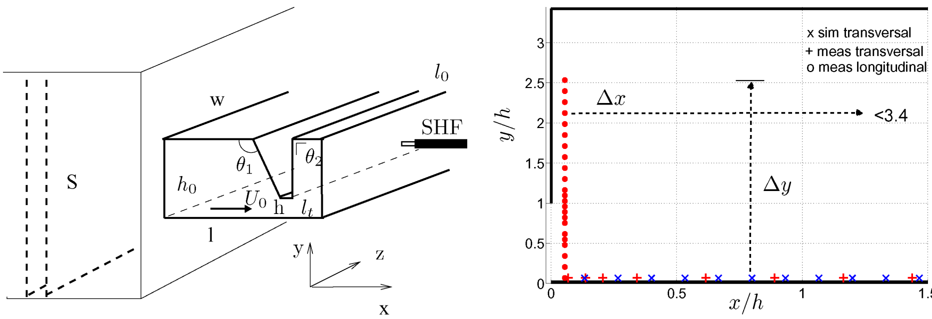

(a) Setup (b) Initial stations

Fig. 2. (a) Schematic illustration of experimental setup and 'in-vitro' teeth-shaped nozzle. Symbols are as defined in Table 1 and Fig. 1 with SHF denoting stationary hot film (SHF) anemometry. The main flow direction is indicated by a bold arrow. (b) Initial data stations for transverse ($y < 0.5$ mm and $\Delta y = 0.1$ mm) and longitudinal ($x < 0.5$ mm $\Delta x = 0.1$ mm) profiles gathered downstream the trailing edge of the teeth, corresponding to $x/h = 0$ and $y/h = 1$, for SHF measurements (transverse $+$, longitudinal $\circ$) are indicated. In addition, transverse profiles taken from simulations ($\times$) for comparison are given as well.

geometry matches the computational grid applied in the numerical simulations except for the channel length upstream the obstacle as seen from Table 1. The upstream channel length in the computational grid yields 80 mm compared to 42 mm in the 'in-vitro' replica.

4.2. *Single sensor anemometry*

Velocity measurements were made by constant temperature anemometry (IFA300) at a Reynolds number $Re = 4000$ based on the inlet height h_0 and the inlet bulk velocity $U_\mathrm{b} = 2.5\,\mathrm{m/s}$ corresponding to a volume airflow rate $\phi = 363\,l/\mathrm{min}$. A single sensor hot film (TSI 1201-20) with a diameter of $50.8\,\mu\mathrm{m}$ and a working length of 1.02 mm was traversed in the x, y and z directions by means of a two-dimensional stage positioning system (Chuo precision industrial co. CAT-C, ALS-250-C2P and ALS-115-E1P). The accuracy of positioning in the longitudinal x and perpendicular y or z direction yields 4 and 2 μm, respectively.

The single sensor hot film was positioned perpendicular to the x direction corresponding to a film yaw angle $\alpha = 0°$. The film position is parallel to the z axis to enhance spatial accuracy in the y direction, except when the two-dimensionality of the flow is verified along the z axis for which the film is parallel with the y axis. The stem was varied to a pitch angle $\beta = 11°$ in order to measure the flow velocity near the wall and to limit flow disturbances induced by the probe stem. The hot-film is calibrated against mean velocities given by a thermal mass flow meter (TSI 4040). A fourth-order polynomial law is fitted to the anemometers output voltage in order to convert the measured voltage to velocity. The measured output voltages are corrected for temperature variations, boundary layer development and wall proximity on a ninth-order convergent nozzle ensuring a top-hat outlet profile and turbulence intensities below 1% [Bruun, 1995; Johnstone *et al.*, 2005]. Applied voltage corrections are well below the obtained accuracy of 0.1 m/s in the velocity range of interest. At each measurement station velocity data are gathered during 4 s consecutively at a sampling frequency of 40 kHz.

4.3. *Measurement Stations*

The near flow field of the jet issuing from the constriction h is experimentally scanned in the longitudinal x-direction and in the traverse y-direction. The initial measurement stations are situated at less as 0.5 mm from the wall coinciding with either the flat bottom plate for the transverse or the trailing teeth edge for the longitudinal profiles as schematically indicated in Fig. 2(b). The displacement Δx and Δy is set to 0.1 mm in order to ensure high spatial accuracy, e.g. 68 measurement stations from the initial station up to $y/h = 1$ in the transverse profile. Transverse data parallel with the y-axis are gathered up to $y/h = 2.5$ or 185 measurements for each initial x-station. All transverse measurement stations are situated between $0 < x < 11\,\mathrm{mm}$ downstream the constriction up to the nozzle exit. The longitudinal direction is scanned from the initial stations up to $x/h = 3.4$, which results in 249 measurement stations for each initial y-station. Consequently, longitudinal measurements are gathered downstream the constriction up to 14 mm in free space downstream the nozzle exit.

5. Results and Discussion

The computed and measured velocity flow field is systematically compared for the measurement stations indicated in Fig. 2(b). This way a detailed comparison of the flow development in the near field from $0 < x/h < 1.5$, i.e. downstream the constriction at $x = 0$ up to the nozzle exit, is obtained. A quantitative comparison of the mean and fluctuation part of the velocity is performed in the next subsections.

Since the anemometry data inform on the magnitude of the velocity, denoted U, and not on a single component, the magnitude of the simulated velocity is considered for the comparison, except when explicitly mentioned.

5.1. *Constriction outlet conditions: initial transverse profile*

The mean and rms of the measured ($x/h = 0.06$) and simulated ($x/h = 0.13$) initial transverse velocity profiles downstream the obstruction, are presented in Fig. 3. Some similarities and dissimilarities between measured and simulated profiles are observed.

The presence of the obstruction on one side and a flat wall on the other side is expected to provoke an asymmetry in the mean velocity profile. This asymmetry is indeed observed in the simulated as well as the measured mean profiles. However, the measured and simulated flow profiles indicate a different flow development due to

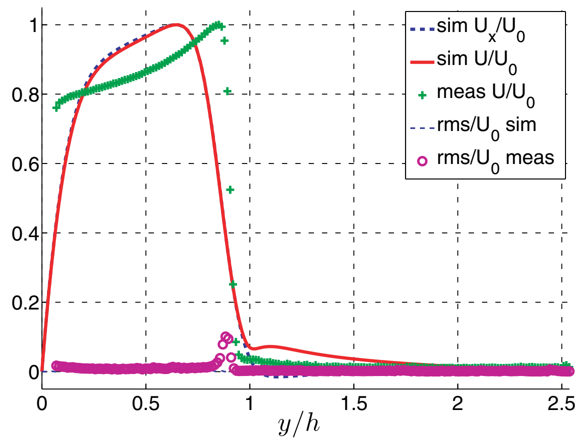

Fig. 3. Mean and fluctuating (rms) portions of the initial measured ($x/h = 0.06$, meas) and simulated ($x/h = 0.13$, sim) transverse velocity profile downstream the obstruction: U denotes the magnitude of the velocity normalised with the maximum velocity in the initial transverse profile U_0 and U_x the component along the x-axis.

the presence of different velocity gradients. It is clearly seen that the mean velocity profile at the outlet can be described roughly by three consecutive growth rates $\mathrm{d}U/\mathrm{d}y$, whereas more are needed to describe the measured profiles. In addition, the position of the maximum velocity U_0 is shifted towards $y/h = 1$ and the overall jet width is significantly larger for the measured data compared to the simulated data. For completeness besides the magnitude also the x-component of the simulated velocity U_x field is plotted. It is seen that for $y/h < 1$ the difference between the magnitude and the U-component is small ($< 1\%$). Although for $y/h \geq 1$ an important discrepancy between both quantities is observed due to the presence of a recirculation zone in which the contribution of the x-component of the velocity is small compared with the y-component. Since the anemometry data are obtained with a single film mounted parallel to the y-axis, the film is less sensitive to the y-component and consequently the measurement less accurate. Therefore, the measured velocity for $y/h \geq 1$ is comprised between the magnitude of the simulated x-component and the magnitude of the velocity simulation.

The overall turbulence level at the outlet is $< 2\%$ for the measured as well as the simulated data. Nevertheless, the asymmetry in the measured mean velocity data is associated with a local turbulence peak exceeding 10%. The absence of such a peak in the simulated data is associated with the different position y_m/h of maximum mean velocity U_0 with respect to the aperture edge at $y/h = 1$.

Therefore, despite the matching geometry and flow conditions for the simulated and measured data, some important differences in the initial outlet profiles downstream the constriction are observed.

5.2. *Transverse mean velocity profiles*

The characterisation of the development of the mean measured and simulated velocity profiles in the near field downstream the constriction is based on the quantities schematically indicated in Fig. 1(b), i.e. $y_\mathrm{m}(x)$ distance from the wall up to maximum flow velocity $U_\mathrm{m}(x)$ and $y_{1/2}(x)$ distance from the wall up to $U_\mathrm{m}(x)/2$. In addition, the jet width Δy_w is sought. The characteristic velocity at the constriction outlet U_0 is defined as the maximum velocity of the initial transverse mean velocity profile discussed in the previous subsection.

The transverse profiles are obtained for downstream positions ranging from the obstruction up to the nozzle exit, i.e. $0 < x/h < 1.5$ as shown in Fig. 2. An overview of the measured and simulated mean velocity profiles is shown in Fig. 4. The growth rate of the jet and the asymmetry of the profiles are sought by considering the downstream evolution of the position $y_\mathrm{m}(x/h)$ corresponding to the maximum velocity $U_\mathrm{m}(x/h)$ for each profile, the outer position $y_{1/2}(x/h)$ corresponding to half the maximum velocity $U_\mathrm{m}/2(x/h)$ and the ratio of the maximum velocity within each profile $U_\mathrm{m}(x/h)$ to the characteristic velocity U_0. The resulting quantities $y_\mathrm{m}(x/h)$, $y_{1/2}(x/h)$ and $U_\mathrm{m}(x/h)/U_0$ are illustrated in Figs. 5(a) and 5(b). The position of maximum velocity $y_\mathrm{m}(x)/h$ is seen to decrease for the measured as well as the

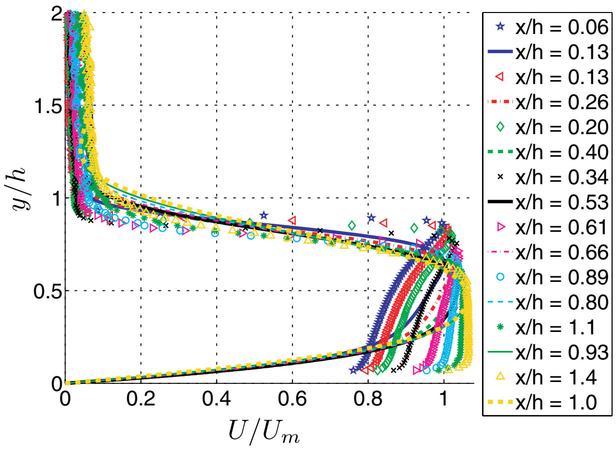

Fig. 4. Measured (symbols) and simulated (lines) transverse mean velocity profiles for $0 < x/h < 1.5$. The magnitude of the profiles normalised with the characteristic velocity U_0 is plotted. U_0 corresponds to the maximum of the initial transverse profile discussed in Sec. 5.1.

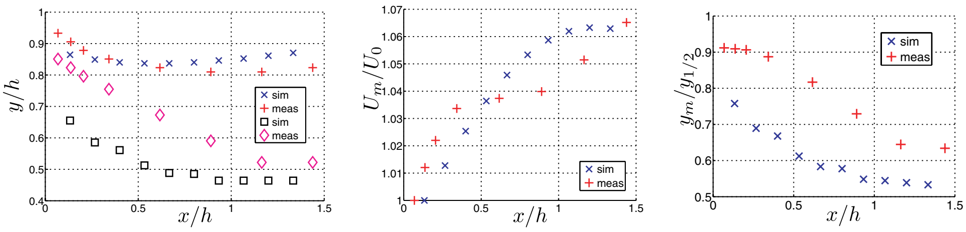

(a) $y_{1/2}(\times, +), y_{\rm m}(\square, \diamond)$ (b) $U_{\rm m}/U_0$ (c) $y_{\rm m}/y_{1/2}$

Fig. 5. Measured (meas) and simulated (sim) downstream evolution, $0 < x/h < 1.5$, for (a) the position of maximum velocity and the outer position of half the maximum velocity $y_{1/2}$ (simulated $= \times$ and measured $= +$) and $y_{\rm m}$ (simulated $= \square$ and measured $= \diamond$), (b) the ratio of the maximum velocity to the characteristic outlet velocity U_m/U_0 and (c) the ratio of the positions y_m and $y_{1/2}$, i.e. $y_m/y_{1/2}$.

simulated profiles. Nevertheless, measured $y_{\rm m}(x)/h$-values continue to decrease until $x/h \geq 1.1$ is reached, whereas a nearly constant value ($\pm 2\%$) is attained for simulations $y_{\rm m}(x/h \geq 0.7)/h \approx 0.47$. So $y_m/h \approx$ constant is postponed on the measured data compared to the simulated data.

The outer position $y_{1/2}$, corresponding to half the maximum velocity $U_{\rm m}$, shows a decrease followed by an increase for both the measured as well as simulated velocity data for increasing x/h-values. Although, the observed increase of $y_{1/2}$ on the measured data, $x/h \geq 1.1$, is postponed with respect to the simulated data, $x/h \geq 0.7$. Moreover, a constant y_m range and increase of $y_{1/2}$ are seen to occur at approximately the same downstream positions x/h, i.e. $x/h \geq 1.1$ and $x/h \geq 0.7$ for the measured and simulated data, respectively.

Figure 5(c) illustrates the resulting ratio $y_m/y_{1/2}$. As before, measured and simulated data exhibit the same overall tendency, i.e. a decrease until a constant value is reached. In addition, again the downstream x/h station for which a constant regime is approximated is postponed when comparing measured to simulated data. The ratio $y_m/y_{1/2}$ is a simple measure on the (a)-symmetry of the jet development. In general the initial decrease of the measured and simulated ratios indicates an increased symmetry of the jet. Note that $y_m/y_{1/2} \approx 0.9$ as observed for the measured profiles immediately downstream the obstacle indicates that y_m and $y_{1/2}$ almost coincides, which indicates a large velocity gradient in the outer layer near the teeth edge. Such a large gradient will favor vorticity stretching for $y/h \approx 1$, whereas a shifted position of maximum velocity towards $y/h \approx 1$ will favor vorticity convection for transverse positions with $y/h \approx 1$.

The ratio $y_m/y_{1/2}$ provides a first quantification of the asymmetry of the jet development. In addition, the evolution of a jet width Δy_w corresponding to a mean velocity larger as a certain percentage p of $U_m(x)$, i.e. $U(y/h, x/h) > p \times U_m(x/h)/100$, is sought. Figure 6 illustrates the jet width Δy_w for percentages derived on the measured transverse velocity profiles. Firstly, for each downstream position $0 < x/h < 1.5$, a variable percentage p is determined for each transverse profile on the first transverse velocity measurement near the wall, i.e. $y/h \leq = 0.07$ as $p(x/h) = U(y/h \leq 0.07, x/h)/U_m(y_m, x/h) \times 100$. Resulting percentages $p(x/h)$ are depicted in Fig. 6(b). The retrieved percentages $p(x/h)$ increase gradually up to 97% from the trailing edge of the obstacle up to the nozzle exit and yield, respectively, 77, 79, 81, 84, 90, 92, 94, 96, 97 and 97%. Secondly, p is fixed to 97%, i.e. the maximum percentage determined by the measured near-wall velocities. Consequently, $\Delta y_w(x/h, p = 97\%)$ involves all transverse measurement stations for which the velocity exceeds $0.97 \times U_m(x/h)$. The fixed percentage $p = 97\%$ is indicated in Fig. 6(b) as well.

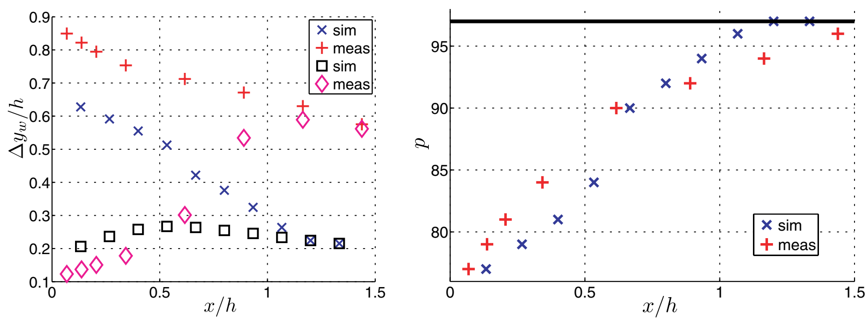

(a) $\Delta y_w(p)$ (b) $p(x/h)$

Fig. 6. The jet width Δy_w for different downstream stations $0 < x/h < 1.5$ is shown in Fig. 6(a) (1) for p fixed to 97% (simulated □, measured ◇) and (2) for variable percentage $p(x/h)$ (simulated ×, measured +) determined on the measured near wall value at $y/h \leq 0.07$ as $U(y/h \leq 0.07, x/h)/U_m(y_m, x/h) \times 100$. The resulting percentages $p(x/h)$ are illustrated in Fig. 6(b) where the fixed percentage $p = 97\%$ is indicated by a solid line.

For $x/h \geq 1$ the variable percentages are close to the fixed percentage $p = 97\%$ so that the resulting jet widths Δy_{w} are approximately the same as can be seen in Fig. 6(a). Consequently, for $x/h \geq 1$ the jet width Δy_{w} observed for $p = 97\%$ on the measured profiles is almost three times the jet width obtained from simulated data. Despite a slight increase-decrease tendency for x/h smaller are greater than 0.6, the jet width Δy_{w} ($p = 97$) observed for the simulated data is fairly constant, i.e. $0.2 < \Delta y_{\mathrm{w}} < 0.28$. For the measured transverse profiles, the jet width is seen to broaden for increasing x/h so that $0.1 < \Delta y_{\mathrm{w}} < 0.6$. A steep increase occurs from $\Delta y_{\mathrm{w}} \approx 0.3$ to $\Delta y_{\mathrm{w}} \approx 0.55$ as $x/h > 0.7$. The initial occurrence of small jet widths $\Delta y_{\mathrm{w}} < 0.2$ is due to the large asymmetry involving a narrow peak superposed on the measured transverse velocity profile for small x/h as is easily observed on the initial profile at $x/h = 0.06$ shown in Fig. 3. This peak is absent in the simulated profiles, so that small $\Delta y_{\mathrm{w}} < 0.2$ are not observed for the simulated transverse profiles. The broadening of Δy_{w} for $x/h > 0.7$ is associated with the disappearance of such a peak.

The percentage p-value set to $p = 97\%$ allows to detect such narrow peaks, but are not suitable to consider the overall jet width. Therefore, the jet width Δy_{w} is re-evaluated with p-values set as $p(x/h) = U(y/h \leq 0.07, x/h)/U_m(y_m, x/h) \times 100$. The resulting jet width Δy_{w} is decreasing with x/h for simulated as well as measured profiles. Despite the general tendency, the decrease more pronounced for the simulated than for the measured data. In addition, Δy_{w} is seen to be 1.3 up to 2.6 times larger for the measured than for the simulated profiles.

5.3. *Transverse rms profiles*

Figure 7 shows the rms values of the measured and simulated velocity profiles for which the mean values are shown in Fig. 4. Simulated rms values are below 2% regardless the spatial position of the measurement station. The measured profiles on the other hand exhibit a peak in the turbulence intensity up to 10% near the obstacle edge. The evolution of the spatial position of the maximum rms value for $0 < x/h < 1.5$ is depicted in Fig. 8(a). As a reference, the position of the maximum mean velocity is indicated for each x/h station as well. The maximum turbulence intensity for the measured profiles shifts from $y/h \approx 0.9$ at $x/h = 0.06$ down to $y/h \approx 0.8$ at $x/h > 0.5$. The maximum mean velocity y_{m} is seen to precede the maximum turbulence intensity, which occurs closer towards the obstacle edge and therefore for larger y/h values. The discrepancy between y_{m} and maximum turbulence position is increasing for $x/h > 0.7$ since y_{m} is decreasing while the maximum turbulence position is maintained. For the simulated profiles on the other hand no peak is observed since the turbulence intensity is below 1%. The maximum values occur for $y/h \approx 0.5$. Although due to the low turbulence intensities, the simulated flow is laminar in contrast to the measured flow for which turbulence is seen to be generated near the edge of the obstacle and is convected downstream.

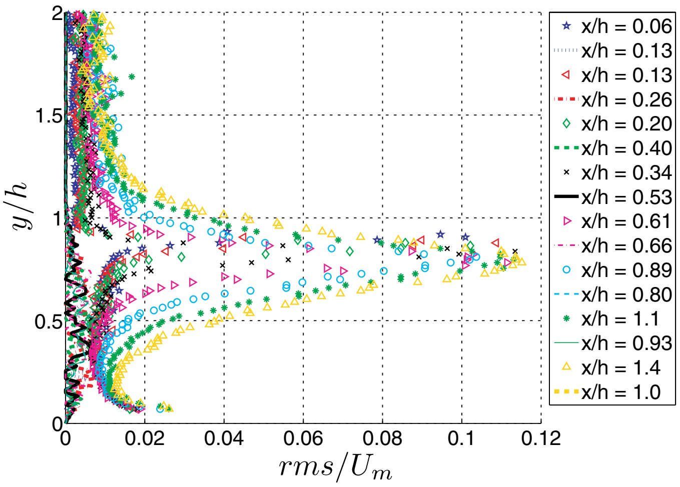

Fig. 7. Turbulence intensities associated to the measured (symbols) and simulated (lines) transverse velocity profiles shown in Fig. 4 for $0 < x/h < 1.5$.

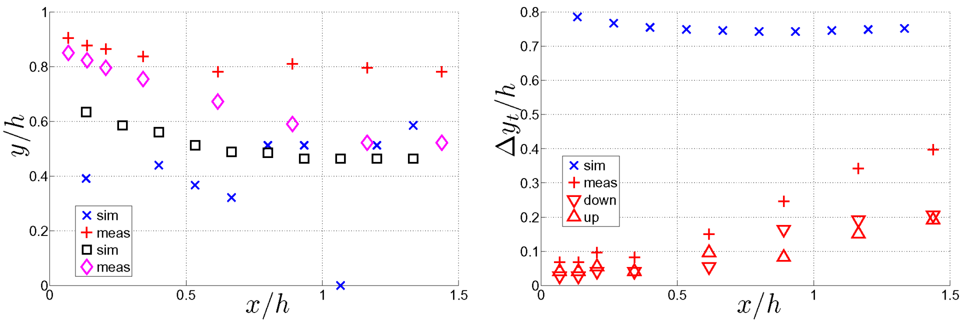

(a) (b)

Fig. 8. (a) Position of maximum turbulence intensity in the measured (+) and simulated (×) profiles shown in Fig. 7 for $0 < x/h < 1.5$. The maximum mean velocity y_m is given for measured (□) and simulated (⋄) profiles. (b) The width of the turbulence peak for half the maximum value, $\Delta y_t/h$, for simulated (×) and measured (+) profiles. For measured profiles the half widths for y/h larger (△) and smaller (▽) than the peak position are indicated as well.

The width of the turbulence peak Δy_t is considered in Fig. 8(b). A narrow turbulence peak, $\Delta y_\mathrm{t}/h < 0.1$, is observed for small $0 < x/h < 0.34$. The peak is seen to broaden gradually up to $\Delta y_\mathrm{t}/h \approx 0.4$ for $x/h = 1.5$. In addition, the symmetry of the turbulence peak is verified by considering the contribution to Δy_t for y/h-values, respectively, larger and smaller than the position of maximum turbulence intensity. Resulting values are indicated in Fig. 8(b). The small turbulence intensities and absence of a peak observed for simulated data result in $\Delta y_\mathrm{t}/h \approx 0.75$ regardless x/h.

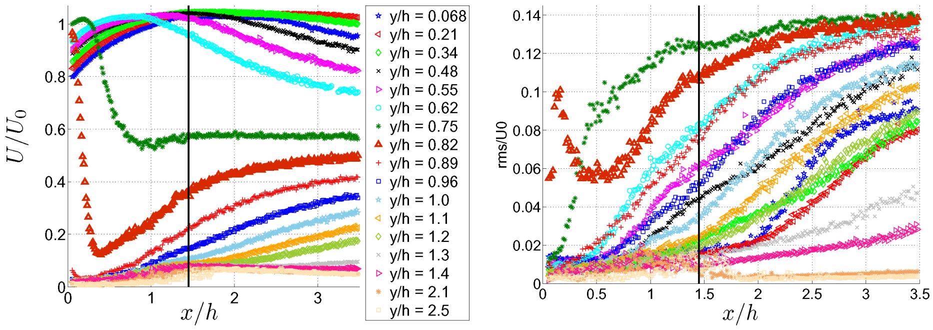

(a) mean (b) rms

Fig. 9. Measured longitudinal (a) mean and (b) rms velocity profiles for the measurement stations indicated in Fig. 2(b). The nozzle exit at $x/h = 1.5$ is depicted by a solid line. Measured values for $y/h \approx 0.82$ ($\triangle$) are indicated in bold.

5.4. *Measured mean and rms longitudinal velocity profiles*

In addition to the transverse velocity profiles, longitudinal velocity profiles are measured for stations with $0 < y/h < 2.5$ and $0 < x/h < 3.5$ as indicated in Fig. 9. The estimated longitudinal mean and rms velocity profiles are given in Fig. 9. In general, the longitudinal profiles confirm the findings for the transverse velocity profiles for $x/h < 1.5$, e.g. the maximum in the mean velocity is seen to shift towards the wall and the jet width is seen to decrease when moving to more downstream observation positions. Although, no quantification is assessed since Δy between two longitudinal profiles is to broad to result in an accurate quantification. Nevertheless, a narrow turbulence peak and steep decrease of mean velocity is observed at $y/h \approx 0.82$ for $x/h < 0.2$.

6. Conclusion

The presented research provides experimental as well as numerical flow data in the near field of a two-dimensional jet issuing from a constriction for a flow with Reynolds number 4000. The constriction is obtained from a teeth-shaped obstacle placed in a rectangular channel so that the current geometrical and flow conditions are relevant to flow through the oral cavity. At term, the current study might contribute to very common applications dealing with a.o. human sound production. It is evident that the considered geometry, although derived from morphological incisor data, does not account for variation of important morphological features such as location, orientation, shape, constriction degree, tissue properties, etc. Nevertheless, to the knowledge of the authors, the current study is the first to account for such a geometry, involving both numerical and experimental flow data enabling one to validate numerical simulations. The near field is studied since a good characterisation is needed in order to describe sound production due to the interaction of an airflow with the obstacle.

A first comparison between simulated and experimental velocity features is obtained by quantifying features typically dealt with in studies of a plane wall jet. This is motivated since the current problem is basically thought of as a two-layer shear flow consisting of an inner layer (similar to a boundary layer) and an outer layer (similar to a free shear layer) as is the case for a plane wall jet. Nevertheless, the current results, numerical as well as experimental, show that the interaction between the two generic layers leads to a more complex near flow field for which more layers can be distinguished. Therefore, future studies should consider the flow field in more detail; i.e. involving both the near and the fully developed region in order to validate established self-similar models and scaling laws for the plane wall jet.

From the comparison of the experimental and simulated flow features, it is seen that the mean flow fields show the same general tendencies, but differ when considering the quantified features. The main common observations for the mean velocity include: (1) the position of maximum velocity y_{m} shifts towards the wall for increasing downstream position, (2) the maximum mean velocity U_{m} increases downstream the constriction, (3) the jet width is seen to decrease for increasing downstream position, (4) as does the ratio of the position of maximum velocity to the outer half width $y_{\mathrm{m}}/y_{1/2}$. Nevertheless, some important differences are observed from the quantified mean velocity features with respect to the structure of the jet: (1) the experimentally observed jet is broadened compared to the numerical jet, (2) the experimental mean velocity exhibits a narrow peak for $y/h \approx 1$, which is absent for the simulated data, (3) the position of maximum velocity is reached for $y/h \approx 1$ on the experimental data, which is larger than for the simulated data and finally (4) the ratio of the position of maximum velocity to the outer half width $y_{\mathrm{m}}/y_{1/2}$ is close to one for the experimental data. The observed differences are the result of increased mean velocity and mean velocity gradients in the vicinity of the teeth edge, i.e. $y/h \approx 1$, for the experimental data compared to the simulated data. Both observations are important considering vorticity. The narrow peak near the teeth edge, observed on the measured mean velocity profiles, is accompanied with a narrow symmetrical peak in turbulence intensity up to 10%. The observed peak is absent in the simulated flow field, which is laminar in the near field downstream the constriction. Consequently, the observed differences in mean and turbulence intensities encourage further research in particular when sound production is of interest. It should be noted that although more accurate measurements can be performed, e.g. by using other measurement techniques, the observed differences largely exceed the uncertainty of the velocity measurements and are therefore significant.

Acknowledgements

The support of the French Rhones-Alpes region and Agence National de la Recherche (ANR) is gratefully acknowledged. X. Grandchamp and A. Van Hirtum like to thank the College Doctoral Franco-Japonais and the Japanese Society for the Promotion of Science (PE07072) for financial support.

References

Bruun, H. [1995] *Hot-Wire Anemometry* (Oxford Science Publications, New York).

Ellis, E. and McNamara, J. [1986] "Cephalometric evaluation of incisor position," *Angle Orthod* 324–344.

Eriksson, J. *et al.* [1998] "An experimental study of a two-dimensional plane turbulent wall jet," *Exp. Fluids* **20**, 50–60.

Fredericks, C. [1974] "A method for determining the maxillary incisor inclination," *Angle Orthod* **44**, 341–345.

Germano, M. *et al.* [1991] "A dynamic subgrid-scale eddy viscosity model," *Phys Fluids A* **3**, 1760–1765.

Guo, Y. *et al.* [2006] "Basic features of the fluid dynamics simulation software Front-Flow/Blue," *JSFM* **58**, 11–15.

Heydecke, G. *et al.* [2004] "Speech with maxillary implant prostheses: ratings of articulation," *J. Dent Res.* **83**, 236–240.

Howe, M. and McGowan, R. [2005] "Aeroacoustics of [s]," *Proc. R. Soc. A* **461**, 1005–1028.

Johnstone, A. *et al.* [2005] "Calibration of hot-wire probes using non-uniform mean velocity profiles," *Exp. Fluids* **39**, 1432–1114.

Kato, C. and Ikegawa, M. [1991] "Large Eddy simulation of unsteady turbulent wake of a circular cylinder using the finite element method," *ASME-FED* **117**, 49–56.

Launder, B. and Rodi, W. [1983] "The turbulent wall jet: measurement and modelling," *Annu. Rev. Fluid Mech.* **15**, 429–459.

Lilly, D. [1992] "A proposed modification of the Germano subgrid-scale closure method," *Phys. Fluids A* **4**, 633–635.

Magne, P. *et al.* [2003] "Anatomic crown width/length ratios of unworn and worn maxillary teeth in white subjects," *J. Prosthetic Dentistry* **89**, 453–461.

McIntyre, G. and Millett, D. T. [2003] "Crown-root shape of the permanent maxillary central incisor," *Angle Orthod* **73**, 710–714.

McIntyre, G. and Millett, D. T. [2006] "Lip shape and position in class II division 2 Malocclusion," *Angle Orthod* **76**, 739–744.

Nozaki, K. *et al.* [2005] "Integration of computational fluid dynamics and computational aero acoustics on grid for dental applications," in *Proc. IEEE CBMS*, p. 6.

Pound, E. [2001] "Utilising speech to simplify a personalised denture service," *Complete Dentures* **28**, 903–908.

Rudolph, D. *et al.* [1998] "The use of tooth thickness in predicting intermaxillary tooth-size discrepancies," *Angle Orthod* **68**, 133–140.

Runte, C. *et al.* [2001] "The influence of maxillary central incisor position in complete dentures on /s/ sound production," *J. Prosthetic Dentistry* **85**, 485–495.

Schierano, G. *et al.* [2001] "Influence of the thickness of the resin palatal vault on the closest speaking space with complete dentures," *J. Oral Rehabilit.* **28**, 903–908.

Shadle, C. [1985] *The Acoustics of Fricative Consonants*, Ph.D. thesis.

Stevens, K. [1998] *Acoustic Phonetics* (MIT Press, London).

Townsend, A. [1999] *The Structure of Turbulent Shear Flow* (Cambridge University Press, UK).

Van Hirtum, A. *et al.* [2009] "Moderate Reynolds number axisymmetric jet development downstream an extended conical diffuser: influence of extension length," *Eur. J. Mech - B/FLUIDS* **28**, 753–760.